

What is the skill of ocean tracers in reducing uncertainties about ocean diapycnal mixing and projections of the Atlantic Meridional Overturning Circulation?

1

Marlos Goes* (1), Nathan M. Urban (1), Roman Tonkonojenkov (1),
Murali Haran (2), Andreas Schmittner (4), and Klaus Keller (1,3)

(1) Department of Geosciences, The Pennsylvania State University, University Park, U.S.A.

(2) Department of Statistics, The Pennsylvania State University, University Park, U.S.A.

(3) Earth and Environmental Systems Institute, The Pennsylvania State University,
University Park, U.S.A.

(4) College of Oceanic and Atmospheric Sciences, Oregon State University, Corvallis, U.S.A.

* Corresponding author e-mail: mpg14@psu.edu

Submitted to **Journal of Geophysical Research - Oceans**

May 13, 2010

Abstract

2 Current projections of the oceanic response to anthropogenic climate forcings are uncer-
3 tain. Two key sources of these uncertainties are (i) structural errors in current Earth
4 system models and (ii) imperfect knowledge of model parameters. Ocean tracers observa-
5 tions have the potential to reduce these uncertainties. Previous studies typically consider
6 each tracer separately, neglect potentially important statistical properties of the system,
7 or use methods that impose rather daunting computational demands. Here we extend and
8 improve upon a recently developed approach using horizontally averaged vertical profiles
9 of chlorofluorocarbon (CFC-11), radiocarbon ($\Delta^{14}\text{C}$), and temperature (T) observations
10 to reduce model parametric and structural uncertainties. Our method estimates a joint
11 probability density function, which considers cross-tracer correlations and spatial auto-
12 correlations of the errors. We illustrate this method by estimating two model parameters
13 related to the vertical diffusivity, the background vertical diffusivity K_{bg} and the upper
14 Southern Ocean mixing u_K_{SO} . The most probable K_{bg} value in the pelagic pycnocline
15 is between 0.1-0.2 cm^2s^{-1} . We show that enhancing u_K_{SO} in the model improves the
16 representations of ocean tracers, as well as improves hindcasts of the Atlantic Meridional
17 Overturning Circulation (AMOC). According to the statistical method, observations of

18 $\Delta^{14}\text{C}$ reduce the uncertainty about K_{bg} the most followed by CFC-11 and T. Using all
19 three tracers jointly reduces the model uncertainty by 40%, more than each tracer individ-
20 ually. Given several important caveats, we illustrate how the reduced model parametric
21 uncertainty improves probabilistic projections of the AMOC.

1. Introduction

22 The North Atlantic Overturning Circulation (AMOC) is a key component of the climate
23 system [*Munk & Wunsch, 1998*]. Past changes in the AMOC intensity are associated with
24 considerable changes in global scale temperature and precipitation patterns [*McManus et*
25 *al., 2004*]. Anthropogenic climate forcings may trigger an AMOC threshold response, with
26 potentially serious impacts on natural systems and human welfare [*Patwardhan, 2007*;
27 *Keller et al., 2000*]. Current AMOC model predictions are deeply uncertain [*Zickfeld et*
28 *al., 2007*; *Meehl et al., 2007*].

29 Tracer observations such as chlorofluorocarbon-11 (CFC-11) and radiocarbon ($\Delta^{14}C$)
30 provide information on the ventilation rate and advective properties in the ocean on time-
31 scales ranging from decadal to centennial that can be used for evaluating the skill of climate
32 models in simulating the ocean circulation [*Doney et al., 2004*]. A better representation
33 of these processes in models can possibly improve AMOC projections.

34 A key variable for determining ocean circulation properties in models is the vertical ocean
35 diffusivity (K_v). Changing this value in model simulations has a large impact on oceanic
36 heat storage and transport, uptake of ocean tracers such as CO_2 [*Sokolov et al., 1998*],
37 and on the work necessary to lift the abyssal waters through stratification (that closes
38 the MOC circulation) [*Wunsch & Ferrari, 2004*]. This variable is highly uncertain [*Munk*
39 *& Wunsch, 1998*], and it is sometimes tuned in models to generate a realistic AMOC
40 strength [*Gao et al., 2003*]. In addition, this parameter value affects the existence of
41 multiple states of the MOC in model simulations [*Schmittner & Weaver, 2001*].

42 Various processes lead to mixing in the ocean such as shear or buoyancy forced turbu-
43 lence, interactions of flow with topography, and double diffusion (differential molecular
44 diffusion of heat and salt). See *Smyth & Moum* [2001] and *Moum & Smyth* [2001] for re-
45 views. Although General Circulation Models have been increasing their ability of parame-
46 terizing subgrid scale turbulent processes in the ocean (*Bryan & Lewis* [1979]; *Pacanowski*
47 *& Philander* [1981]; *Large et al.* [1994]; *Ferrari et al.* [2008]), due to the complexity of
48 the problem and processes involved, most schemes are still highly simplified and param-
49 eterized. In Earth System Models of Intermediate Complexity (EMICs), the absence of
50 more complex parameterizations elevates the importance of the parameters related to K_v
51 in order to fulfill the model necessity of turbulent mixing in simulating a realistic AMOC
52 strength.

53 Several studies [e.g. *England*, 1993; *Gao et al.*, 2003] analyze the importance of the
54 magnitude of the diffusivity strength and parameterization on the MOC structure and
55 representations of tracers in ocean models. These studies are typically silent on the
56 question of how much information is contained in the different types of observations. This
57 is an important question, for example, to inform the design of AMOC observation and
58 prediction systems [cf. *Baehr et al.*, 2008; *Keller et al.*, 2007].

59 *Schmittner et al.* [2009] discusses a relatively simple but computationally efficient
60 method to estimate the background ocean diffusivity K_{bg} from the combination of spa-
61 tially resolved ocean tracer observations considering both, observational and model errors.
62 However, *Schmittner et al.* [2009] neglects the effects of cross-correlation between different
63 tracers, which limits the number of tracers that can be combined in a joined probability
64 density function. In another recent study, *Bhat et al.* [2009] estimates the posterior prob-

65 ability distribution for K_{bg} using $\Delta^{14}\text{C}$ and CFC-11 observations. Their approach uses a
66 Gaussian process emulator for the climate model and estimates the distribution of K_{bg}
67 via a Bayesian approach. While their kernel mixing based approach to constructing the
68 emulator is flexible and efficient, it is conceptually complex and computationally highly
69 demanding for routine use with more than two ocean tracers.

70 Here we estimate the probability density function (pdf) of K_{bg} using three tracers si-
71 multaneously. Our approach provides a fast and easy way to implement the methodology,
72 enabling the routine use of information from several ocean tracers jointly, while still con-
73 sidering spatial autocorrelation as well as cross-correlation between residuals of different
74 tracers. We demonstrate how neglecting cross-correlation and/or simplifying the mean
75 function can compromise the accuracy of the estimation. We improve the treatment of
76 uncertainties surrounding K_v in the model by considering the structural uncertainty about
77 the upper Southern Ocean mixing (u_K_{SO}). We show that an ensemble with enhanced
78 Southern Ocean mixing is more consistent with the observations.

79 Furthermore, we advance on previous work by quantifying and ranking the skill of the
80 tracers CFC-11, $\Delta^{14}\text{C}$ and temperature (T) to constrain the uncertainties in the model
81 parameter K_{bg} . We demonstrate the potential utility of the considered observations to
82 improve model predictions of the AMOC.

2. Methods

2.1. Earth System Model of Intermediate Complexity

83 We use the University of Victoria Earth System Model of Intermediate Complexity
84 (UVic 2.8; *Weaver et al.* [2001]). In the UVic model, we parameterize the diapycnal
85 diffusivity as $K_v = K_{tidal} + K_{SO} + K_{bg}$, which consists of the diffusivity due to local

86 dissipation of tidal energy and its resulting generation of turbulence and mixing (K_{tidal} ,
87 *Simmons et al.* [2004]), a parametrization for the vigorous mixing (K_{SO}) observed in the
88 Southern Ocean [e.g. *Naveira Garabato et al.*, 2004], plus a background diffusivity K_{bg}
89 that represents all other processes that lead to mixing, such as non-local dissipation of
90 tidal energy, mesoscale eddy activity, double diffusion, hurricanes, interaction of flow with
91 topography, and others.

92 The model accounts for increased mixing over rough topography based on the tidal
93 mixing scheme of *St. Laurent et al.* [2002], and uses the *Gent & McWilliams* [1990]
94 eddy mixing parameterization. It is likely that K_{bg} is spatially and temporally variable
95 in nature [*Sriver et al.*, 2010], but due to a lack of a more explicit representation of the
96 processes and for simplicity we assume a constant value of K_{bg} everywhere. Note that
97 K_{tidal} decays exponentially (with an e-folding depth of 500 m above the sea floor) such
98 that it is unimportant in the pelagic pycnocline (i.e., away from the boundaries). However,
99 it is the value of K_{bg} in the pelagic pycnocline that is most important in determining the
100 large scale ocean circulation in models [c.f., *Marotzke*, 1997; *Munk & Wunsch*, 1998]. For
101 the Southern Ocean (south of 40S) parametrization, the vertical mixing is truncated at
102 $1 \text{ cm}^2/\text{s}$ as a lower bound ($K_{SO} > 1 \text{ cm}^2/\text{s}$). The Southern Ocean is one of the most
103 tempestuous oceans on earth, and these transient effects may produce strong turbulent
104 mixing, specially in the upper Southern Ocean. We denote the K_{SO} mixing in the upper
105 500 meters of the water column by u_K_{SO} throughout the manuscript.

106 We create two ensembles to analyze the uncertainty in two model parameters, the
107 background ocean diffusivity (K_{bg}) and the upper Southern Ocean diffusivity (u_K_{SO}).
108 Each ensemble contains seven members, corresponding to a grid of the parameter K_{bg}

109 values of (0.05, 0.1, 0.15, 0.2, 0.3, 0.4, and 0.5) cm^2s^{-1} . The difference between the two
110 ensembles is that in the first one (ENSEMBLE 1), the enhanced upper SO mixing is not
111 applied, so it is equal the mixing in the rest of the upper ocean ($u_K_{SO}=0$), whereas
112 the second one (ENSEMBLE 2) uses an enhanced mixing in the entire column of the
113 Southern Ocean ($u_K_{SO}=1$).

114 The ocean component in UVic is MOM2 [*Pacanowski, 1995*] with a $1.8^\circ \times 3.6^\circ$ reso-
115 lution in the horizontal and 19 depth levels. The atmospheric component is a one-layer
116 atmospheric energy-moisture balance model, which does not apply flux correction and
117 is forced by prescribed winds from the NCAR/NCEP climatology. Also included in the
118 model are a thermodynamic sea-ice component, a terrestrial vegetation (TRIFFID), and
119 an oceanic biogeochemistry based on the ecosystem model of *Schmittner et al.* [2005].

120 The model is spun up from observed data fields as initial conditions for 3000 years
121 (with a coupled carbon cycle for the last 1000 years) for each parameter value. It is then
122 integrated from years 1800-2100 using historical and projected climate forcings (SRES-
123 A1FI scenario), extended to the year 2200 following *Zickfeld et al.* [2008]. We modify
124 the model to include non- CO_2 greenhouse gases, volcanic and sulfate forcings from *Sato*
125 *et al.* [1993] and *Hansen & Sato* [2004]. Atmospheric sulfates data enter the model as
126 gridded optical depth [*Koch et al., 1999*], and follow the same rate of decrease as the CO_2
127 concentration after 2100.

2.2. Data

128 We focus on a subset of observations that have previously been shown to provide con-
129 straints on the parameterization of K_v in ocean models: (i) temperature (T), (ii) chlo-
130 rofluorocarbon 11 (CFC-11), and (iii) radiocarbon ($\Delta^{14}\text{C}$) observations [cf. *Schmittner et*

131 *al.*, 2009; *Bhat et al.*, 2009; *Toggweiler et al.*, 1989]. $\Delta^{14}\text{C}$ is defined as the $^{14}\text{C}/^{12}\text{C}$ ratio
132 of air-sea fractionation-corrected data [*Stuiver & Polach*, 1977]. Each of the tracers in this
133 subset has a different behavior, and can constrain K_v in different ways. The temperature
134 observations constrain K_v , because K_v affects, for example, the shape of the thermocline
135 as well as the penetration of the anthropogenic heat anomalies [*Gnanadesikan*, 1999]. The
136 $\Delta^{14}\text{C}$ observations can constrain K_v in two main ways, because it has a natural and an
137 anthropogenic component. The natural component can provide information of mixing
138 rates (that are, in turn, a function of K_v) in the order of centuries or millennia. The
139 anthropogenic component, which greatly increased during the 1950s and 1960s due to
140 thermonuclear explosions, provides information on decadal time-scale. Here we do not
141 make distinction between natural and bomb ^{14}C , thus we use its total concentration.
142 The anthropogenic tracer CFC-11 also constrains K_v on decadal time-scale, because at-
143 mospheric emissions started in the 1930s. The solubility of CFCs in water is dependent
144 on the temperature. Considering CFC-11 and $\Delta^{14}\text{C}$ jointly can provide new insights into
145 vertical oceanic mixing because they have very different forcing histories, air-sea equili-
146 bration timescales and water solubility [*Broecker & Peng*, 1974; *Ito et al.*, 2004], and the
147 observation errors and signal-to-noise ratios of the two tracers are different. We analyze
148 published data products for these three tracers [*Locarnini et al.*, 2006; *Key et al.*, 2004]
149 and average the model hindcasts over the time the observations have been collected, i.e.,
150 1990's for CFC-11 and $\Delta^{14}\text{C}$, and 1950-2000 for temperature. We interpolate the obser-
151 vations to the model grid and the model output is restricted to the regions where the data
152 products are available. All considered ocean tracer observations are horizontally averaged
153 into global mean vertical profiles.

154 Further, we compare the ocean tracers information with information from the climato-
 155 logical AMOC strength at 24°N calculated from observations with the inverse model of
 156 *Lumpkin & Speer* [2003], which is estimated as $(17.6 \pm 2.7 \text{ Sv})$. The model ensembles are
 157 calibrated against observations using a Bayesian inference method. We assume a Gaus-
 158 sian likelihood function and estimate the posterior probability of K_{bg} and $u_{K_{SO}}$ given
 159 the observations through a Markov Chain Monte Carlo (MCMC) method [*Metropolis et*
 160 *al.*, 1953]. Our method accounts for auto-correlations of the residuals, as well as cross-
 161 correlation between residuals of different tracers. For this, a separable covariance matrix
 162 Σ is estimated. The inversion and the numerical implementation of the calibration pro-
 163 cedure are detailed in the next subsection. Readers not interested in the details of the
 164 statistical inversion technique can skip the next subsection without loss of understanding.

2.3. Bayesian model inversion

165 The goal of Bayesian parameter estimation is to infer a probability distribution(s) $p(\theta|O)$
 166 representing the uncertainty in one (or more) climate model parameter θ , conditional on a
 167 vector of observed data O . Here θ are parameters K_{bg} and $u_{K_{SO}}$, which are related to the
 168 vertical ocean diffusivity in UVic. The inferential procedure is based on a statistical model
 169 that relates the model parameters (θ) to the observations (O) by way of the ensemble of
 170 model output $M(\theta)$. The statistical model used here assumes that the observations are
 171 randomly distributed around the model prediction, according to

$$O = M(\theta) + \epsilon, \quad (1)$$

172 where the error is a random variable drawn from a multivariate normal distribution

$$\epsilon \sim N(\mu, \Sigma), \quad (2)$$

173 with an unknown mean or bias term μ and covariance matrix Σ . These distributional
 174 parameters are estimated along with the model parameter θ . The error term encompasses
 175 all processes which may cause the observations to deviate from the model predictions,
 176 including model structural error, unresolved variability in the climate system, and mea-
 177 surement error. Because these errors are uncertain, they are modeled stochastically as
 178 a random process, approximated here by a potentially correlated Gaussian probability
 179 function.

180 The error mean term μ represents model bias, which is common for each observed
 181 variable across ensemble members. *Schmittner et al.* [2009] assumed a bias which is
 182 constant with depth. Here we expand upon this form by using a general linear form that
 183 varies with depth (z), $\mu = a + bz$. This form improves the model fit as indicated by
 184 a exploratory data analysis in the next section. The covariance matrix, described later,
 185 captures the residual variability that is unaccounted by the linear bias term.

186 The above probability model describing the spread of observations about the model
 187 output defines a likelihood function $L(O|\theta, \mu, \Sigma)$ for the data conditional on the model
 188 and covariance parameters:

$$L(O|\theta, \mu, \Sigma) = (2\pi)^{-N/2} |\Sigma|^{-1/2} \exp\left(-\frac{1}{2} \tilde{r}^T \Sigma^{-1} \tilde{r}\right), \quad (3)$$

189 where Σ is a covariance matrix and $\tilde{r} = O - M(\theta) - \mu$ are the bias-corrected data-model
 190 residuals.

191 Consider an ensemble M containing p runs of a climate model, where each run corre-
 192 sponds to a different value of a climate model parameter, θ_k , $k = 1, \dots, p$. For each ensem-
 193 ble member we analyze n ocean tracer profiles defined at d spatial locations (depths). The
 194 matrix Σ is $nd \times nd$ specifying the covariance between n tracers at d locations (depths).
 195 Assuming separability, Σ can be approximated by a Kronecker product of two matrices:

$$\Sigma = \Sigma_T \otimes C_S + \Sigma_M, \quad (4)$$

196 where Σ_T corresponds to the $n \times n$ cross-covariance matrix of the tracers, and C_S is
 197 the $d \times d$ spatial correlation matrix (in depth) respectively. Σ_M is the data measurement
 198 error which we assume to be negligible compared to the other errors because of the spatial
 199 aggregation of the data.

200 The cross-covariance matrix Σ_T depends on $n(n-1)/2$ cross-tracer correlation coef-
 201 ficients ρ_{ij} (since $\rho_{ij} = \rho_{ji}$), and on residual standard deviations σ_i of the n individual
 202 tracers:

$$\Sigma_T = \begin{bmatrix} \sigma_1^2 & \sigma_1\sigma_2\rho_{12} & \dots & \sigma_1\sigma_n\rho_{1n} \\ \sigma_2\sigma_1\rho_{21} & \sigma_2^2 & \dots & \sigma_2\sigma_n\rho_{2n} \\ \vdots & \vdots & \ddots & \vdots \\ \sigma_n\sigma_1\rho_{n1} & \dots & \dots & \sigma_n^2 \end{bmatrix}. \quad (5)$$

203 We model the spatial correlation C_S using a Gaussian correlation function, a special
 204 case of the Matérn class of covariance functions (see, for e.g., *Stein* [1999]). This function
 205 decays with distance between locations d_i and d_j with a correlation length scale λ , assumed
 206 to be the same for all tracers:

$$(C_S)_{ij} = \exp\left(-\frac{|d_i - d_j|^2}{\lambda^2}\right). \quad (6)$$

207 Given the property of the Kronecker product (see, for example, *Lu & Zimmerman*
208 [2005]), the multivariate normal likelihood function $L(y, \theta)$ becomes:

$$L(O|\theta, \mu, \Sigma_T, C_S) = (2\pi)^{-N/2} (|\Sigma_T|^d |C_S|^n)^{-1/2} \exp \left[-\frac{1}{2} \tilde{r}^T (\Sigma_T^{-1} \otimes C_S^{-1}) \tilde{r} \right], \quad (7)$$

209 where $N = nd$ is the total number of data points, and $\tilde{r} = [O_1 - M_1 - \mu_1, \dots, O_n - M_n - \mu_n]^T$
210 is the concatenated vector containing the misfit between the unbiased model predictions
211 and the corresponding observations for the considered tracers. The Kronecker structure
212 of Equation 4 allows the $nd \times nd$ matrix Σ to be efficiently inverted by inverting the two
213 smaller matrices Σ_T ($n \times n$) and C_S ($d \times d$).

214 Once the probability model has been specified in the form of a likelihood function, the
215 Bayes' theorem allows inference about the posterior distribution of θ . The theorem states
216 that the posterior probability of the unknown parameters is proportional to their prior
217 probability distribution, multiplied by the likelihood of the data, according to:

$$p(\theta, a, b, \sigma, \rho, \lambda|O) \propto L(O|\theta, a, b, \sigma, \rho, \lambda) p(\theta) p(a) p(b) p(\sigma) p(\rho) p(\lambda). \quad (8)$$

218 We draw 20,000 samples from the above posterior distribution by a Markov chain Monte
219 Carlo (MCMC) algorithm. The MCMC algorithm jointly estimates the model parameters
220 ($\theta = K_{bg, u} K_{SO}$), $2n$ bias coefficients (a_i and b_i), n standard deviations (σ_i), $n(n-1)/2$
221 cross-tracer correlations (ρ_{ij}), and one correlation length (λ). This is an improvement
222 upon the methodology of *Schmittner et al.* [2009] which held all parameters but θ fixed at
223 optimized values, and did not consider the uncertainty in the other parameters. Because
224 the model output is only defined on a discrete grid of values, the MCMC algorithm

225 proposes discrete jumps for the parameters θ during its random walk through parameter
 226 space, and continuous moves for all other parameters.

227 We choose a uniform prior $p(\theta)$ for the model parameters K_{bg} and $u_K K_{SO}$. For the
 228 correlation length we apply the lognormal prior $\ln \lambda \sim N(5.5, 0.5^2)$, such that the loga-
 229 rithm of λ is normally distributed with mean 5.5 and standard deviation 0.5. This prior
 230 locates most of the probability mass of the distribution between 0 and 600 meters. We use
 231 normal priors for the bias parameters a_i and b_i , $p(a_i) = N(0, (\sigma_i/\lambda)^2)$ and $p(b_i) = N(0, \sigma_i^2)$.
 232 For the estimate of individual tracers distributions, where the cross-correlation matrix is
 233 a scalar (i.e. $\Sigma = \sigma_1^2$), we use a Jeffreys prior ($p(\sigma_i) \propto 1/\Sigma$). When the multi-tracer
 234 cross-covariance matrix is estimated, we specify an inverse Wishart prior distribution
 235 $\Sigma_T \sim IW(S, \nu)$, with a diagonal scale matrix $S = I$ and $\nu = 2n + 1$ degrees of freedom.
 236 A diagonal scale matrix reduces spurious correlations by penalizing tracer residuals which
 237 are are not independent of each other. Spurious correlation is not a problem when the
 238 data dimension is large, but when the data are sparse such a regularization procedure is
 239 prudent (see, for instance, *Barnard et al.* [2000] or Chapter 19 in *Gelman et al.* [2003],
 240 and references therein).

Equation (8) provides the joint posterior probability of both the model parameter and
 the bias and covariance parameters. The marginal posterior probability of the model
 parameter alone is obtained by integrating the joint posterior over all other parameters:

$$p(\theta|O) = \int p(\theta, a, b, \sigma, \rho, \lambda|O) da db d\sigma d\rho d\lambda. \quad (9)$$

241 Since the posterior is estimated by MCMC sampling, this posterior distribution of θ is
 242 easily obtained by simply considering the θ samples while ignoring the samples for the
 243 other parameters.

3. Results

3.1. Effect of ocean diapynal diffusivity on the AMOC hindcasts and spatial fields

244 In the adopted model the AMOC strength is positively correlated with the parameters
245 K_{bg} and $u_{K_{SO}}$ (Figure 1). K_{bg} has a strong influence on the model hindcasts of the
246 maximum AMOC strength, while the AMOC sensitivity to $u_{K_{SO}}$ is weaker. The range
247 of AMOC strength varies from about 5–23 Sv across all simulations. The inclusion of
248 enhanced upper Southern ocean mixing ($u_{K_{SO}} = 1$), can increase the AMOC by a few
249 Sverdrups, with more influence at lower K_{bg} . Under the projected climate forcings, the
250 AMOC strength decreases in most cases, but it is more sensitive (in absolute values) to
251 the considered forcings for higher diffusivity values. Due to the strong dependence of the
252 AMOC structure and behavior on the values of the parameters K_{bg} and $u_{K_{SO}}$ in this
253 model, a reduction in the parametric uncertainty has the potential to improve AMOC
254 hindcast and projection in the model.

255 The different parameter values result in different hindcasts of ocean tracers such as CFC-
256 11 (Figure 2) and $\Delta^{14}\text{C}$ (Figure 3), due to the different tracers advection and diffusion rates
257 in the model. Higher K_{bg} values result in stronger vertical water exchange, increased deep
258 water mass formation, which carries water with higher tracer content from the surface, and
259 decreased vertical stratification in the ocean. $u_{K_{SO}}$ broadly produces the same effects
260 of K_{bg} . Nevertheless, $u_{K_{SO}}$ impacts more heavily the lower K_{bg} runs and the Southern
261 Ocean stratification.

262 Here we analyze the tracers concentrations as vertical profiles of their averaged con-
263 centrations over the globe. We consider three different observations, CFC-11, $\Delta^{14}\text{C}$ and
264 T (Figure 4, shown as an example for ENSEMBLE 1). In general, the observations are

265 contained by the model ensemble spread, except for T in the deep ocean, which is too
266 cold in the model.

3.2. The uncertainty of the statistical inversion

267 The inversion method use the information contained in the tracers to estimate the
268 model parameter K_{bg} , taking into account uncertainties in $u_{K_{SO}}$. Key improvements
269 compared to *Schmittner et al.* [2009] are: (i) the estimation of the cross-correlation terms;
270 (ii) a more refined representation of structured biases in the Likelihood function; and
271 (iii) the consideration of the effects of the structural uncertainty (specifically about the
272 implementation of mixing in the SO). Here we demonstrate how these improvements affect
273 the joint posterior pdf of the model parameters. We test the sensitivity of the method to
274 the choice of the statistical (or nuisance) parameters for the distribution of K_{bg} . In this
275 sensitivity test, we do not account for uncertainties in the parameter $u_{K_{SO}}$. Therefore,
276 we only use outputs from ENSEMBLE 1.

277 For illustration, we use two tracers, $\Delta^{14}C$ and T, as input for the statistical inversion.
278 We calculate four inversion, which vary the number of statistical parameters to be esti-
279 mated. The structure of the errors which differ from each other by the representation
280 of two main parameters, the bias and the cross-correlation of the residuals between the
281 model and the observations. The bias term represents our guess of the mean function
282 of the residuals. We demonstrate the trade-off between complexity of the bias-correction
283 and the covariance structure of the residuals in a simple sensitivity study.

284 Specifically, we analyze four different assumptions about the structural error terms.
285 First, we use a simple case where the bias is constant and there is no residuals cross-
286 correlation; second, we use a constant bias and estimate the cross-correlation; third we

287 estimate a linear bias but no residual cross-correlation; and fourth, in which linear bias
 288 and cross-correlation are both estimated. To summarize the experiments in the sensitivity
 289 study, we have: a) $\mu = b$, $\rho = 0$, b) $\mu = b$, $\rho = \hat{\rho}$, c) $\mu = ax + b$, $\rho = \hat{\rho}$, and d) $\mu = ax + b$,
 290 $\rho = \hat{\rho}$. Note that the calibration also estimates standard deviation, correlation length and
 291 the model parameter, as described in Section 2. Comparing all pdfs (Figure 5) we see
 292 that for the individual pdfs the representation of the bias term can be essential for the
 293 model parameter estimation. When a more simplified bias ($\mu = b$) is applied (Figures 5a
 294 and 5b), the pdfs in this example are displaced toward higher K_{bg} values, and centered
 295 on 0.3 and 0.4 cm^2s^{-1} . In contrast, in the linear bias estimations, the mode of K_{bg} pdf is
 296 centered around 0.15 and 0.2 cm^2s^{-1} . For the cases with linear bias (cases c and d), the
 297 standard deviation of the residuals of both tracers (Table 1) decrease in comparison to
 298 the constant biases cases (cases a and c). On the other hand, the standard deviations of
 299 the residuals are not influenced by the addition of cross-correlation parameters.

300 The inclusion of the cross-correlation parameter impacts the position of the joint pos-
 301 terior (black curves), and its strength is closely related to the representation of the bias.
 302 When the bias has a better representation, which is the linear bias case here (Figures 5c
 303 and 5d), the cross-correlation term has little influence on the joint pdf. A comparison of
 304 the strength of the cross-correlation parameters (cases (b) and (d) in Table 2) shows that
 305 $\rho = 0.70$ when μ is constant, and is much smaller $\rho = 0.40$ when μ is linear. Comparing
 306 the posteriors of the cases (b) and (d) (Figures 5b and 5d), ρ can visibly change the
 307 posterior when the mean function is less structured. Case (b) shows a counterintuitive
 308 result where the posterior mode is distant from the modes of the individual components
 309 (Figure 5b). This result indicates that with a relatively poor representation of the mean

(bias) function, considering or neglecting the effects of this residual cross correlation can drastically change the K_{bg} posterior estimate. This effect becomes less pronounced, as the representation of the model bias term improves (eg. Figure 5b vs. Figure 5c). As discussed by *Cressie* [1993] (pp. 25), “What is one person’s (spatial) covariance structure may be another person’s mean structure”. In other words, there is a trade-off between estimating a mean function for the tracer residuals to account for structural model errors and the magnitude of the residual cross correlation across the considered sources of information.

3.3. Estimating the uncertainty of vertical diffusivity

The analysis so far illustrates how different tracers observations can be combined to reduce uncertainty about one mixing parameter (K_{bg}). This reduction in parametric uncertainty results, at least in the framework of the adopted model, in a reduction of the prediction uncertainty about the AMOC. Of course, there are several caveats associated with structural errors and other neglected uncertainties in this study. We return to this issue in the section Caveats, below. In this section we illustrate how this information can potentially be used to reduce uncertainties in two model parameters and improve model hindcasts and projections of the AMOC. Here the inversion uses our best estimate of the model bias term (linear), and accounts for cross-tracer correlation. We make three inversions (6), one to estimate K_{bg} for the ENSEMBLE 1, a second to estimate K_{bg} for the ENSEMBLE 2, and a third inversion which uses information from both ensembles to generate probability distributions for K_{bg} and $u_K K_{SO}$ in a Bayesian model average fashion.

Information from the three considered tracers, CFC-11, T and $\Delta^{14}C$, is introduced in the statistical inversion for the estimation of uncertainties in the model parameters. For

332 comparison, we also show the K_{bg} pdf for the climatological AMOC observations in Figure
333 6. The K_{bg} pdf is derived from estimate of the climatological AMOC strength of *Lumpkin*
334 *& Speer* [2003] by assimilating a single data point assuming a normally distributed error.
335 In principle, the model could be calibrated with both the ocean tracers and AMOC
336 strength data by using the derived AMOC pdf as a prior for K_{bg} . However, this would
337 neglect potential correlations between ocean tracer and AMOC strength residual errors.
338 As a proper treatment of AMOC/tracer correlations is beyond the scope of this work, we
339 present the AMOC-derived pdf just for comparison, without assimilating it in the joint
340 posterior pdf.

341 The tracers distributions of both ensembles show similar behavior. Nevertheless, the
342 ENSEMBLE 1 (figure 6a) has in general higher K_{bg} modes in comparison to ENSEMBLE
343 2 (figure 6b). This result is expected, since ENSEMBLE 2 has additional mixing over the
344 upper Southern Ocean, and therefore more energy is transferred into the system (*Munk*
345 *& Wunsch* [1998]). The projection of the AMOC distribution over the K_{bg} space (lines
346 with triangles), are also displaced to lower values in ENSEMBLE 2, because ENSEMBLE
347 2 has stronger AMOC values for the same K_{bg} (figure 1)

348 When information from both ensembles are added together (figures 6c and 6d), the
349 ENSEMBLE 2 dominates the Markov chain for $\Delta^{14}C$ and T, with probabilities of 100 %
350 and 65 % for ENSEMBLE 2, respectively. Conversely, CFC-11 has 80% probability of
351 happening ENSEMBLE 1 (figure 6d). The joint posterior of all tracers encompassing the
352 two ensembles (figure 6c) is entirely described by ENSEMBLE 2, therefore the posteriors
353 in figures 6b and 6c are practically identical.

354 When all the two model parameters are assimilated jointly (figure 6c), the considered
355 sources of information have rather different skill in improving K_{bg} estimates and AMOC
356 predictions (see Table 2 for the properties of the statistical distributions). $\Delta^{14}\text{C}$ has the
357 highest information content with respect to improving K_{bg} estimates, its posterior 95 %
358 credible interval (CI) is the tightest ($0.21 \text{ cm}^2\text{s}^{-1}$) in comparison to the other tracers.
359 CFC-11 comes in second, with a 95 % CI of $0.24 \text{ cm}^2\text{s}^{-1}$, and T comes last with the
360 largest CI of $0.26 \text{ cm}^2\text{s}^{-1}$.

361 Combining the information of the three considered tracers (line with squares in Figure
362 6c), favors K_{bg} values in the lower part of the considered range, from $0.1\text{--}0.2 \text{ cm}^2\text{s}^{-1}$.
363 Note that the joined probability density function is narrower than each individual pdf
364 indicating an advantage of using multiple tracer observations in reducing the parameter
365 uncertainty.

366 As discussed in previous studies [e.g. *Schmittner et al.*, 2009], the K_{bg} value in a coarse
367 resolution ocean model represents the effects of background diffusivity combined with
368 subgridscale diffusivity (i.e., a model shortcoming). Hence, even if our estimate does not
369 represent directly the observed estimates of pelagic diffusivity of $0.1 \text{ cm}^2\text{s}^{-1}$ [*Ledwell et*
370 *al.*, 1993], they are closer to its value when regional mixing properties are added to the
371 model.

3.4. AMOC projections

372 The joint posterior K_{bg} and $u_{-}K_{SO}$ estimates (figures 6c and 6d) can be used to derive
373 model projections of the AMOC in 2100 and 2200 (Figure 7). The model hindcast for the
374 maximum AMOC strength in 2000 is about $15\text{--}15.5 \text{ Sv}$. In 2100, the expected strength for

375 the AMOC in this model is about 11 Sv. In 2200 the AMOC shows a slight strengthening
376 relative to the 2100 conditions with an expected value of roughly 12 Sv.

377 The K_{bg} and u_K_{SO} estimates suggest an AMOC hindcast for the year 2000 (Figure 7)
378 that is about 2 Sv weaker than the climatological AMOC estimates of *Lumpkin & Speer*
379 [2003]. The inclusion of the parameter u_K_{SO} in the analysis reduces significantly the
380 discrepancy of the AMOC estimates relative to the K_{bg} (Figure 6c). Other systematic
381 model bias(es), such as too weak buoyancy forcing (e.g. from errors in the simulation
382 of the atmospheric hydrological cycle and surface freshwater fluxes) can compromise the
383 estimates of the current and projected AMOC strength for the Uvic model. Further
384 discussion and implications are described in the next section.

4. Caveats

385 Our results are subject to many caveats. These caveats point to potentially fruitful
386 research directions. In the statistical part, we consider only highly aggregated data.
387 Basinwide zonal averages could, for example, provide potentially useful information on
388 where the model performs better. In the projection part, other model parameters, such
389 as those affecting the response of the ocean-atmosphere coupled system, for example, the
390 hydrological cycle [*Saenko & Weaver, 2004*], climate sensitivity or sensitivity of climate
391 to aerosol concentrations, [cf. *Tomassini et al., 2007; Forest et al., 2002*], are also highly
392 uncertain, and can impact (probably widen) probabilistic AMOC projections and should
393 be considered. In addition, the atmospheric model in UVic is rather simplified, and
394 neglects important ocean-atmosphere feedbacks.

395 UVic does not use flux correction. Freshwater flux correction is known to improve the
396 salinity and stratification in ocean models [*Sorensen et al.*, 2001], and can be used to
397 improve projections and hindcasts.

398 In the hindcasts part, we show how including regional aspects of vertical mixing can
399 improve the representation of the AMOC. The model parameters uncertainties need to be
400 estimated together as performed here, since addition of new parameters can change the
401 structure of the other calibrations. *Jayne* [2009] describes, “this is the typical conundrum:
402 it is difficult to assess whether any of the given parameterizations improve the model
403 since comparing to observational metrics may obscure compensating errors in different
404 parameterizations”.

5. Conclusion

405 We develop and apply a computationally efficient and statistically sound method to
406 rank and quantify the skill of different sources of information to reduce the uncertainty
407 about ocean model parameters and the resulting climate predictions. We improve on
408 previous work by (i) refining the estimation of errors in the model structure, (ii) including
409 several ocean tracers and two model parameters at once in a computationally efficient
410 fashion, and (iii) quantifying and ranking the skill of different sources of information to
411 reduce the uncertainty about a model parameter. Subject to the aforementioned caveats,
412 we show how $\Delta^{14}\text{C}$, CFC-11, and T together sharpen the estimates of K_{bg} by 40 % and
413 improve AMOC projections in the UVic model.

414 The K_{bg} derived from individual observations (i.e., $\Delta^{14}\text{C}$, CFC-11, T) are broadly con-
415 sistent, but show slight discrepancies that we attribute predominantly to structural model
416 errors. Of the considered observations, $\Delta^{14}\text{C}$ has the highest skill in reducing uncertainties

417 in AMOC projections, but it is also the most distant from the pdf observational derived
418 AMOC estimates. $\Delta^{14}C$ is followed (in decreasing skill of being able to reduce K_{bg} uncer-
419 tainty) by CFC-11 and T. The second parameter analysed in this work, $u_{-}K_{SO}$ improved
420 the representations of C14 and T in the model, and improves the representation of the
421 AMOC strength.

422 AMOC projections show a reduction of the maximum of the joint posterior in 2100
423 by roughly 25% (3.5 Sv). Perhaps both surprisingly and encouraging, the pdfs of K_{bg}
424 estimated in this study are quite similar among the considered ocean tracers and the two
425 ensembles analyzed, which have different different representations of the upper Southern
426 Ocean mixing and AMOC. This convergence of K_{bg} estimates based on different sources
427 of information and parameterizations suggest that K_{bg} can be robustly estimated from
428 the oceanic tracers studied here.

429 **Acknowledgments.** We thank Mike Eby, Damon Matthews, Bob Key and Ray Najjar
430 for helpful discussions and feedback. This work is partially supported by the National
431 Science Foundation as well as by the U.S. Department of Energy's Office of Science (BER)
432 through the Northeastern Regional Center of the National Institute for Climatic Change
433 Research. Any errors and opinions are those of the authors alone.

References

- 434 Baehr, J., D. McInerney, K. Keller, and J. Marotzke (2008), Optimization of an observing
435 system design for the North Atlantic meridional overturning circulation, *J. of Atmos.*
436 *and Ocean. Tech.*, **25**, 625–634.
- 437 Barnard, J., R. McCulloch and X. Meng (2000), Modeling covariance matrices in terms
438 of standard deviations and correlations with application to shrinkage, *Statistica Sinica*,
439 **10**, 1281–1311.
- 440 Bhat, K.S., Haran, M., Tonkonojekov, R., and Keller, K. (2009), Inferring likelihoods
441 and climate system characteristics from climate models and multiple tracers. *Annals of*
442 *Applied Statistics.*, *in revision*. Available at <http://www.geosc.psu.edu/~kkeller>.
- 443 Broecker, W.S., and T.H. Peng (1987), Gas exchange rates between air and sea. *Tellus*,
444 **26**, 21–35.
- 445 Bryan, K., and L.J. Lewis (1979), A water mass model of the world ocean. *J. Geophys.*
446 *Res.*, **84**(C5), 2503–2517.
- 447 Bryan, F. O., G. Danabasoglu, P. R. Gent, and K. Lindsay (2006), Changes in ocean
448 ventilation during the 21st century in the CCSM3. *Ocean Model.*, **15**, 141–156.
- 449 Cressie, N.A. (1993), *Statistics for Spatial Data*, Wiley, New York, 900 pp.
- 450 Dalan, F., P.H. Stone, and A.P. Sokolov (2005), Sensitivity of the Oceans Climate to
451 Diapycnal Diffusivity in an EMIC. Part II: Global Warming Scenario. *J. Climate*, **18**,
452 24822496.
- 453 Danabasoglu, G., J. C. McWilliams, and P. R. Gent (1994), The role of mesoscale tracer
454 transports in the global ocean circulation. *Science*, **264**, 1123–1126.

- 455 Doney et al. (2004), Evaluating global ocean carbon models: The importance of realistic
456 physics. *Glob. Biogeochem. Cycles*, **18**, GB3017, doi:10.1029/2003GB002150.
- 457 England, M. H. (1993), Representing the global-scale water masses in ocean general cir-
458 culation models. *J. Phys. Oceanogr.*, **23**, 1523–1552.
- 459 Ferrari, R., J. C. McWilliams, V. M. Canuto, M. Dubovikov (2008), Pa-
460 rameterization of eddy fluxes near oceanic boundaries. *J. Climate*, **21**, 2770-
461 2789,doi:10.1175/2007JCLI1510.1.
- 462 Chris E. Forest, Peter H. Stone, Andrei P. Sokolov, Myles R. Allen, and Mort D. Webster
463 (2002), Quantifying Uncertainties in Climate System Properties with the Use of Recent
464 Climate Observations. *Science*, **295** (5552), 113. [DOI: 10.1126/science.1064419].
- 465 Gao, Y., H. Drange, and M. Bentsen (2003), Effects of diapycnal and isopycnal mixing
466 on the ventilation of CFCs in the North Atlantic in an isopycnal coordinate OGCM.
467 *Tellus*, **55B**, 837–854.
- 468 Gelman, A., J.B. Carlin, H. S. Stern, and D. B. Rubin (2003), Bayesian Data Analysis,
469 second edition. London: CRC Press.
- 470 Gent, P. R., and J. C. McWilliams (1990), Isopycnal mixing in ocean circulation models.
471 *J. Phys. Oceanogr.*, **20**, 150–155.
- 472 Gent, P. R., F. O. Bryan, G. Danabasoglu, K. Lindsay, D. Tsumune, M. W. Hecht, and
473 S. C. Doney (2006), Ocean Chlorofluorocarbon and Heat Uptake during the Twentieth
474 Century in the CCSM3. *J. Climate*, **19**, 2366–2381.
- 475 Gnanadesikan, A. (1999), A simple predictive model for the structure of the oceanic
476 pycnocline. *Science*, **283**, 2077–2079.

- 477 Hansen, J., and M. Sato (2004), Greenhouse gas growth rates. *Proc. Natl. Acad. Sci.*,
478 USA 101, 16109–16114.
- 479 Ito, T., J. Marshall, and M. Follows (2004), What controls the uptake of tran-
480 sient tracers in the Southern Ocean? *Glob. Biogeochem. Cycles*, **18**, GB2021,
481 doi:10.1029/2003GB002103.
- 482 Jayne, S.R. (2009) The Impact of Abyssal Mixing Parameterizations in an Ocean General
483 Circulation Model. *J. Phys. Oceanogr.*, **39**, 17561775.
- 484 Keller, K., Tan, K., Morel, F.M.M. and Bradford, D.F. (2000), 'Preserving the ocean
485 circulation: Implications for climate policy'. *Climatic Change*, **47**, 17–43.
- 486 Keller, K., C. Deutsch, M. G. Hall and D. F. Bradford (2007), Early detection of changes
487 in the North Atlantic meridional overturning circulation: Implications for the design of
488 ocean observation systems. *J. Climate*, **20**, 145–157.
- 489 Key, R.M., A. Kozyr, C.L. Sabine, K. Lee, R. Wanninkhof, J. Bullister, R.A. Feely, F.
490 Millero, C. Mordy, T.-H. Peng (2004), A global ocean carbon climatology: Results from
491 Global Data Analysis Project (GLODAP). *Glob. Biogeochem. Cycles*, **18**(4), GB4031,
492 doi: 10.1029/2004GB002247.
- 493 Koch, D., D. Jacob, I. Tegen, D. Rind, and M. Chin (1999), Tropospheric sulfur simulation
494 and sulfate direct radiative forcing in the Goddard Institute for Space Studies general
495 circulation model, *J. Geophys. Res.- Atmos.*, 104 (D19), 23,79923,822.
- 496 Large, W. G., J. C. McWilliams, and S. C. Doney (2004), Oceanic vertical mixing: a
497 review and a model with nonlocal boundary layer parameterisation, *Rev. Geophys.*, **32**,
498 363–403.

- 499 Ledwell, J. R., A. J. Watson, and C. S. Law (1993), Evidence for slow mixing across the
500 pycnocline from an open-ocean tracer-release experiment. *Nature*, **364**, 701–703.
- 501 Locarnini, R. A., A. V. Mishonov, J. Antonov, T. Boyer, and H. E. Garcia (2006), World
502 Ocean Atlas 2005. Volume 1: Temperature, 182 pp, U.S. Government Printing Office,
503 Washington, D.C.
- 504 Lu, Nelson and Zimmerman, Dale L. (2005), The likelihood ratio test for a separable
505 covariance matrix. *Stat. & Prob. Lett.*, **73**(4), 449–457
- 506 Lumpkin, R. and K. Speer (2003), Large-scale vertical and horizontal circulation in the
507 North Atlantic Ocean. *J. of Phys. Oceanogr.*, **33**(9), 1902–1920.
- 508 Marotzke J., 1997: Boundary mixing and the dynamics of three-dimensional thermohaline
509 circulation. *J. Phys. Oceanogr.*, **27**, 1713–1728.
- 510 Matsumoto, K. and R. M. Key (2004), Natural Radiocarbon Distribution in the Deep
511 Ocean. *Global Environmental Change in the Ocean and on Land*, Eds., M. Shiyomi et
512 al., pp. 45–58.
- 513 McManus, J.F., Francois, R., Gherardi, J.M., Keigwin, L.D. and Brown-Leger, S. (2004),
514 Collapse and rapid resumption of Atlantic meridional circulation linked to deglacial
515 climate changes. *Nature*, **428**, 834–837.
- 516 Meehl, G.H., T.F. Stocker, W.D. Collins, P. Friedlingstein, A.T. Gaye, J.M. Gregory, A.
517 Kito, R. Knutti, J.M. Murphy, A. Noda, S.C.B. Raper, I.G. Watterson, A.J. Weaver
518 and Z.-C. Zhao (2007), Global climate projections. *Climate Change 2007: The Physical
519 Science Basis*. Contribution of Working Group I to the Fourth Assessment Report of
520 the Intergovernmental Panel on Climate Change, S. Solomon, D. Qin, M. Manning, Z.
521 Chen, M. Marquis, K.B. Averyt, M. Tignor and H.L. Miller, Eds., Cambridge University

- 522 Press, Cambridge, 747–846.
- 523 Metropolis, N., A.W. Rosenbluth, M.N. Rosenbluth, A. H. Teller and E. Teller (1953),
524 Equation of state calculations by fast computing machines. *J. of Chem. Phys.*, **21**,
525 1087–1092.
- 526 Moum, J.N. and W.D. Smyth, 2001: "Upper Ocean Mixing", En-
527 cyclopedia of Ocean Sciences, Academic Press. Available at:
528 <http://salty.oce.orst.edu/smyth/papers/UpOcMixing.pdf>
- 529 Munk W. and Wunsch, C. (1998), Abyssal Recipes-II: Energetics of Tidal and Wind
530 Mixing. *Deep Sea Res.*, **13**, 1977–2010
- 531 Naveira Garabato, A. C., K. L. Polzin, B. A. King, K. J. Heywood and M. Visbeck (2004),
532 Widespread intense turbulent mixing in the Southern Ocean, *Science*, **303**, 210–213.
- 533 Pacanowski, R., and S.G.H. Philander (1981), Parameterization of vertical mixing in
534 numerical models of tropical oceans. *J. Phys. Oceanogr.*, **11**, 1443–1451.
- 535 Pacanowski, R.C. (1995), MOM 2 documentation: Users guide and reference manual,
536 Version 1.0. GFDL Ocean Group Technical Report No. 3, Geophysical Fluid Dynamics
537 Laboratory, Princeton, New Jersey.
- 538 Patwardhan, A., S. Semenov, S. Schneider, I. Burton, C. Magadza, M. Oppenheimer,
539 B. Pittock, A. Rahman, J. Smith, A. Suarez, F. Yamin, K. Keller, A. Todorov, A.
540 Finkel, D. MacMynowski, M. Mastrandrea, M. Fuessel, J. Corfee-Morlot, R. Sukumar,
541 J.-P. van Ypersele, and J. Zillman (2007), Assessing key vulnerabilities and the risk
542 from climate change, Chapter 19 in the Intergovernmental Panel on Climate Change
543 Fourth Assessment Report, Working group II: Impacts, Adaptation and Vulnerability,
544 Cambridge University Press.

- 545 Saenko, O. A. and A. J. Weaver (2004), What drives heat transport in the Atlantic:
546 Sensitivity to mechanical energy supply and buoyancy forcing in the Southern Ocean.
547 *Geophysical Research Letters*, **31**, L20305, doi:10.1029/2004GL020671.
- 548 Sato, M., J.E. Hansen, M.P. McCormick, and J.B. Pollack (1993), Stratospheric aerosol
549 optical depth, 1850–1990. *J. Geophys. Res.*, **98**, 22987–22994.
- 550 Schmittner, A., N.M. Urban, K. Keller, and D. Matthews (2009), Using tracer observations
551 to reduce the uncertainty of ocean diapycnal mixing and climate carbon-cycle projec-
552 tions. *Global Bio. Cycles.*, in press, available at <http://www.geosc.psu.edu/~kkeller>.
- 553 Schmittner, and A. J. Weaver (2001), Dependence of multiple climate states on ocean
554 mixing parameters. *Geophys. Res. Lett.*, **28**, 1027–1030.
- 555 Schmittner, A., A. Oschlies, X. Giraud, M. Eby, and H. L. Simmons (2005), A global
556 model of the marine ecosystem for long-term simulations: Sensitivity to ocean mixing,
557 buoyancy forcing, particle sinking, and dissolved organic matter cycling. *Glob. Bio-
558 geochem. Cycles*, **19**(3), GB3004, doi: 10.1029/2004GB002283.
- 559 Simmons, H. L., S. Jayne, L. St. Laurent, A. Weaver (2004), Tidally driven mixing in a
560 numerical model of the ocean general circulation, *Ocean Modelling*, **6** (3-4), 245–263,
561 ISSN 1463-5003, DOI: 10.1016/S1463-5003(03)00011-8.
- 562 Smyth, W.D. and J.N. Moum, 2001: "3D Turbulence", En-
563 cyclopedia of Ocean Sciences, Academic Press. Available at:
564 <http://salty.oce.orst.edu/smyth/papers/OceanTurbulence.pdf>
- 565 Sokolov, A., C. Wang, G. Holian, P. Stone, and R. Prinn (1998), Uncertainty in the
566 oceanic heat and carbon uptake and its impact on climate projections. *Geophys. Res.
567 Lett.*, **25**, 3603–3606.

- 568 Sorensen, J., J. Ribbe, and G. Shaffer (2001), Antarctic intermediate water mass formation
569 in ocean general circulation models. *J. Phys. Oceanogr.*, **31**, 3295–3311.
- 570 Striver, R. L., Goes, M., Mann, M. E.; Keller, K. (2010), Climate response to tropical
571 cyclone-induced ocean mixing in an Earth system model of intermediate complexity. *J.*
572 *Geophys. Res.* (in press)
- 573 Stein, Michael Leonard (1999), Interpolation of Spatial Data: Some Theory for Kriging,
574 Springer-Verlag Inc., 247 pp.
- 575 St. Laurent, L., H. L. Simmons, S. R. Jayne (2002), Estimating tidally driven mixing in
576 the deep ocean. *Geophys. Res. Lett.*, , **29**, 2106–2110, doi:10.1029/2002GL015633.
- 577 Stuiver, M. & Polach, H.A (1977), "Discussion: Reporting of ^{14}C data", Radiocarbon,
578 **19**, no. 3, pp. 355–363.
- 579 Toggweiler, J.R., Dixon, K., and Bryan, K. (1989), Simulations of radio-carbon in a
580 coarse-resolution, world ocean model, II. Distributions of bomb-produced ^{14}C . *J. Geo-*
581 *phys. Res.*, 94, 8243–8264.
- 582 Tomassini, L., P. Reichert, R. Knutti, T. F. Stocker and M. Borsuk (2007), Robust
583 Bayesian uncertainty analysis of climate system properties using Markov chain Monte
584 Carlo methods, *Journal of Climate*, **20**, 1239–1254.
- 585 Weaver, A.J., M. Eby, E. C. Wiebe, C. M. Bitz, P. B. Duffy, T. L. Ewen, A. F. Fanning,
586 M. M. Holland, A. MacFadyen, H.D. Matthews, K.J. Meissner, O. Saenko, A. Schmit-
587 tner, H. Wang and M. Yoshimori (2001), The UVic Earth System Climate Model:
588 Model description, climatology, and applications to past, present and future climates.
589 *Atmosphere-Ocean*, **39**(4), 361–428.

- 590 Wunsch, C., and R. Ferrari (2004), Vertical Mixing, Energy, and the General Circulation
591 of the Oceans. *Ann. Rev. Fluid Mech.*, **36**, 281–314.
- 592 Zickfeld, K., A. Levermann, M. Morgan, T. Kuhlbrodt, S. Rahmstorf, and D. Keith (2007),
593 Expert judgements on the response of the Atlantic meridional overturning circulation
594 to climate change. *Climatic Change*, **82**, 235–265
- 595 Zickfeld, K., M. Eby, and A.J. Weaver (2008), Carbon-cycle feedbacks of changes in
596 the Atlantic meridional overturning circulation under future atmospheric CO₂. *Glob.*
597 *Biogeochem. Cycles*, **22**, GB3024, doi:10.1029/2007GB003118.

List of Figure Captions

598 **Figure 1.** AMOC strength (Sv), defined as the maximum of the transport streamfunc-
 599 tion, from years 1800 to 2200. Dashed lines are for the ENSEMBLE 1 ($u_K_{SO} = 0$); solid
 600 lines are for the ENSEMBLE 2 ($u_K_{SO} = 1$).

601 **Figure 2.** Zonal averages for the Atlantic Ocean of CFC-11 concentration in [pmol/Kg]
 602 (colorbars) and density anomalies in [Kg/m^3] (contour lines) for the model with diffu-
 603 sivity of $K_{bg} = 0.05$ (top panels) and $K_{bg} = 0.5$ (middle panels). The left column is for
 604 ENSEMBLE 1 ($u_K_{SO} = 0$) and right column for ENSEMBLE 2 ($u_K_{SO} = 1$). The bottom
 605 panel shows the observations from [Key et al., 2004] and [Locarnini et al., 2006].

606 **Figure 3.** Zonal averages for the Atlantic Ocean of $\Delta^{14}\text{C}$ concentration in permil (col-
 607 orbars) and density anomalies in [Kg/m^3] (contour lines) for the model with diffusivity of
 608 $K_{bg} = 0.05$ (top panels) and $K_{bg} = 0.5$ (middle panels). The left column is for ENSEMBLE
 609 1 ($u_K_{SO} = 0$) and right column for ENSEMBLE 2 ($u_K_{SO} = 1$). The bottom panel shows
 610 the observations from [Key et al., 2004] and [Locarnini et al., 2006].

611 **Figure 4.** Global averaged profiles of CFC-11 [Key et al., 2004], $\Delta^{14}\text{C}$ [Key et al., 2004]
 612 and T [Locarnini et al., 2006], for the observations (gray dots) and model ENSEMBLE 1
 613 (colored lines). The legend for the model K_{bg} values is the same as in Figure 1.

614 **Figure 5.** Sensitivity of the model parameter estimation to different treatments of
 615 structural model errors. Shown are the posterior probability density function of $\Delta^{14}\text{C}$
 616 (red lines with crosses) and T (blue lines with circles), and the joint posterior using both

617 observations (black line with squares). The pannels are for the cases discussed in the text:
618 a) $\mu = b$; b) $\mu = b$ and ρ c) $\mu = az + b$; d) $\mu = az + b$ and ρ .

619 **Figure 6.** Posterior probability density function of the model parameters for all con-
620 sidered sources of information, the joint posterior using all available information from
621 observations (line with squares). The climatological AMOC estimate of [*Lumpkin &*
622 *Speer, 2003*] is plotted for comparison (line with triangles). The K_{bg} estimates are for
623 a) ENSEMBLE 1, b) ENSEMBLE 2, c) ENSEMBLE 1 + ENSEMBLE 2; d) the u_K SO
624 estimate is for ENSEMBLE 1 + ENSEMBLE 2

625 **Figure 7.** Joint posterior probability density function of model projections of the
626 maximum AMOC strength in the years 2000, 2100 and 2200 using information from the
627 $\Delta^{14}\text{C}$, CFC-11 and T observations. The climatological AMOC estimate of [*Lumpkin &*
628 *Speer, 2003*] is added for comparison (line with triangles).

Table 1. Properties of the statistical distributions of the sensitivity test for the best K_{bg} : mode, bias ($\mu = az + b$), standard deviation and cross-correlation of residuals for $\Delta^{14}\text{C}$ and T, and mode of the posterior (joint distribution considering all tracers information).

Exp.	Mode (cm^2s^{-1})		bias (a,b)		σ		Cross-corr. at best K_{bg}	Mode of posterior
	$\Delta^{14}\text{C}$	T	$\Delta^{14}\text{C}$	T	$\Delta^{14}\text{C}$	T		
a)	0.3	0.4	(-14.0,0)	(0.45,0)	12.5	0.6	–	0.3
b)	0.3	0.4	(-14.0,0)	(0.45,0)	12.5	0.6	0.70	0.2
c)	0.15	0.2	(-16.1,9e-3)	(0.22,3.3e-4)	7.7	0.28	–	0.15
d)	0.15	0.2	(-16.1,9e-3)	(0.22,3.2e-4)	7.7	0.28	0.40	0.15

Table 2. Properties of the statistical distributions (mode, mean and 95% credible interval [CI] (cm^2s^{-1})) of K_{bg} (figure 6c) for each considered sources of information, the posterior (joint distribution considering all tracers information), and the climatological AMOC estimate (*Lumpkin & Speer [2003]*). Also shown are the cross-tracers correlation at the best K_{bg} value estimated in the joint posterior.

Observation	Mode	Mean	95% CI	Cross-corr. at best K_{bg}		
				$\Delta^{14}\text{C}$	CFC-11	T
$\Delta^{14}\text{C}$	0.15	0.15	0.22	1	0.06	0.38
CFC-11	0.20	0.23	0.26	–	1	0.02
T	0.15	0.18	0.26	–	–	1
posterior	0.15	0.16	0.17	–	–	–
AMOC clim	0.20	0.20	0.42	–	–	–

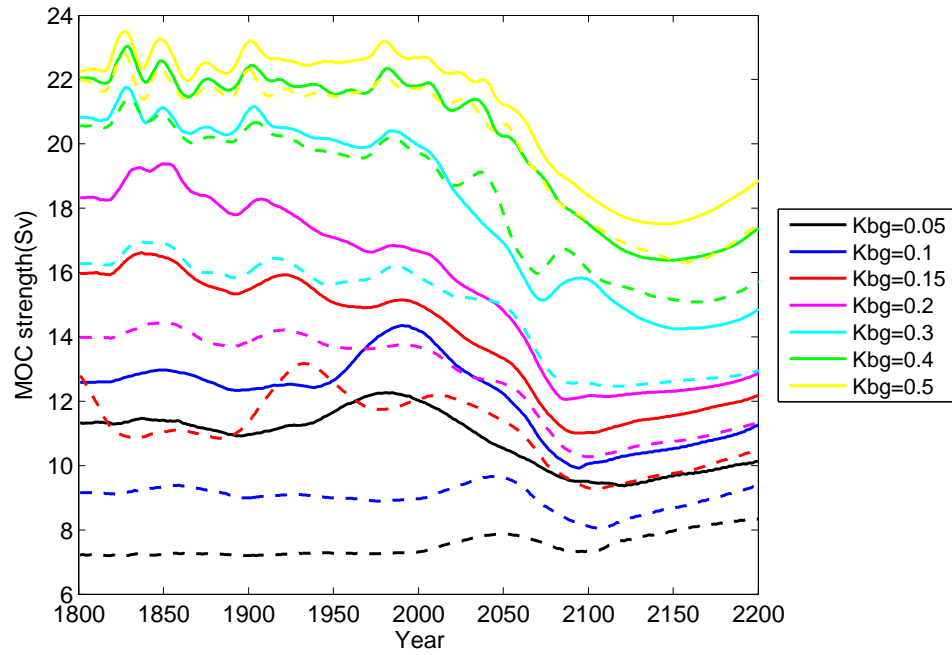


Figure 1. AMOC strength (Sv), defined as the maximum of the transport streamfunction, from years 1800 to 2200. Dashed lines are for the ENSEMBLE 1 ($u_{K_{SO}} = 0$); solid lines are for the ENSEMBLE 2 ($u_{K_{SO}} = 1$).

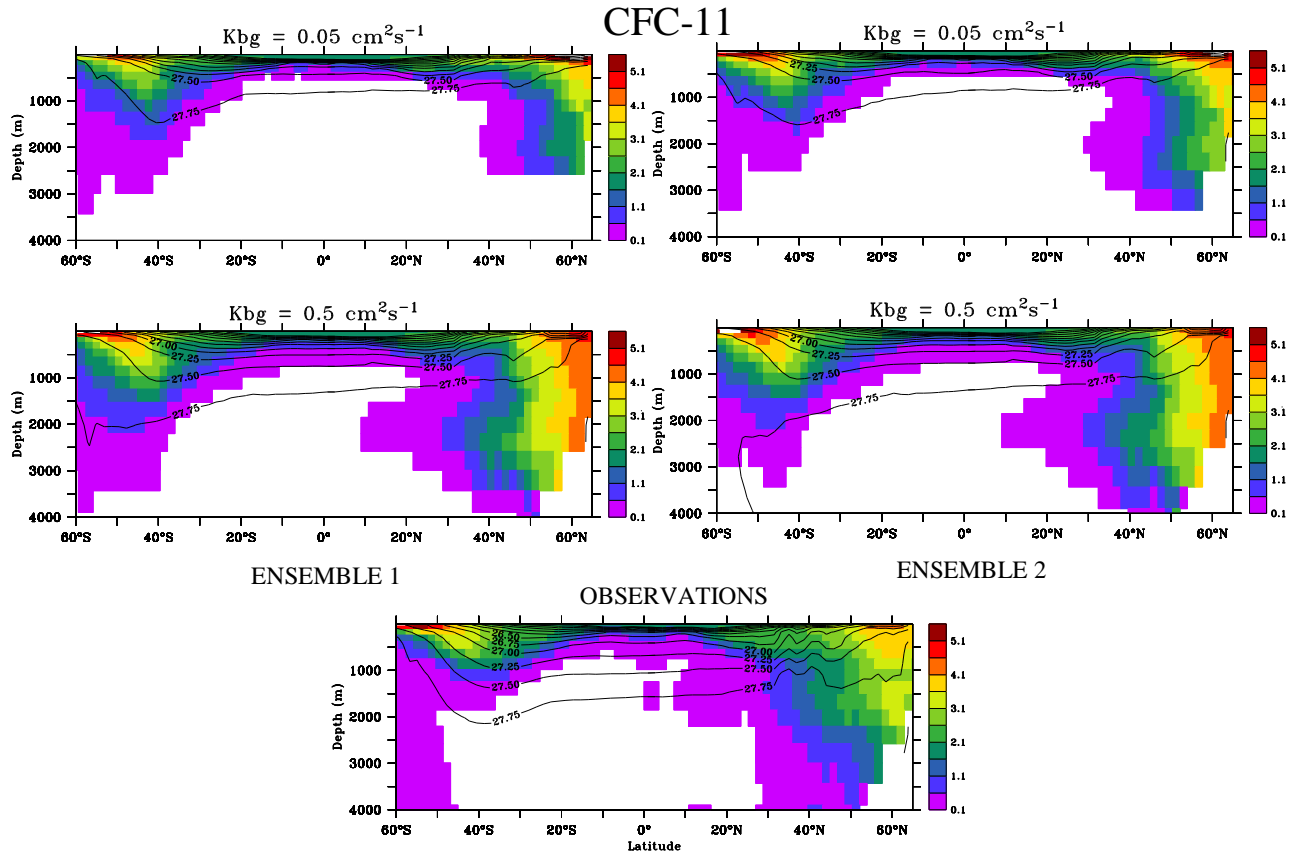


Figure 2. Zonal averages for the Atlantic Ocean of CFC-11 concentration in [pmol/Kg] (colorbars) and density anomalies in [Kg/m³] (contour lines) for the model with diffusivity of $K_{bg} = 0.05$ (top panels) and $K_{bg} = 0.5$ (middle panels). The left column is for ENSEMBLE 1 ($u_{K_{SO}}=0$) and right column for ENSEMBLE 2 ($u_{K_{SO}}=1$). The bottom panel shows the observations from [Key *et al.*, 2004] and [Locarnini *et al.*, 2006].

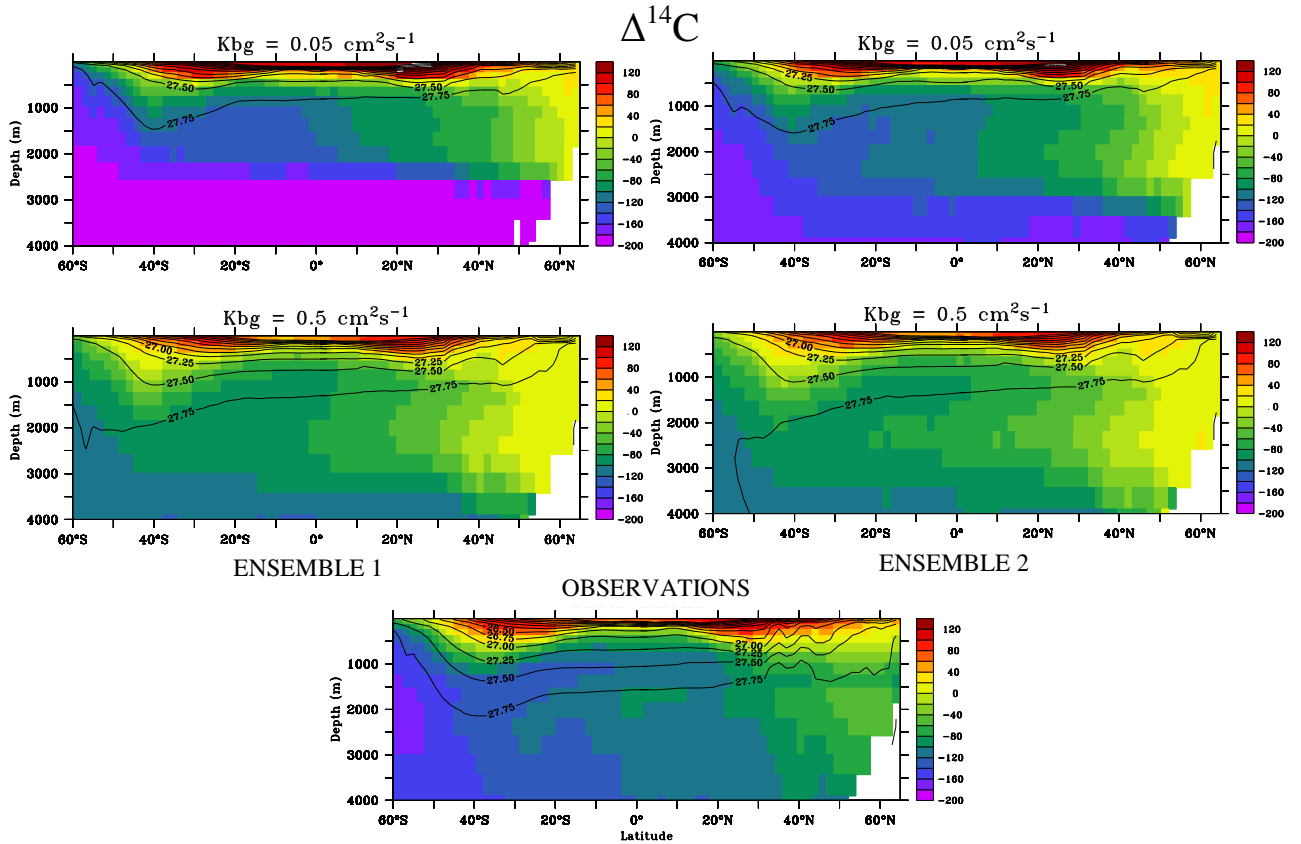


Figure 3. Zonal averages for the Atlantic Ocean of $\Delta^{14}\text{C}$ concentration in permil (colorbars) and density anomalies in $[\text{Kg}/\text{m}^3]$ (contour lines) for the model with diffusivity of $K_{bg} = 0.05$ (top panels) and $K_{bg} = 0.5$ (middle panels). The left column is for ENSEMBLE 1 ($u_{K_{SO}}=0$) and right column for ENSEMBLE 2 ($u_{K_{SO}}=1$). The bottom panel shows the observations from [Key et al., 2004] and [Locarnini et al., 2006].

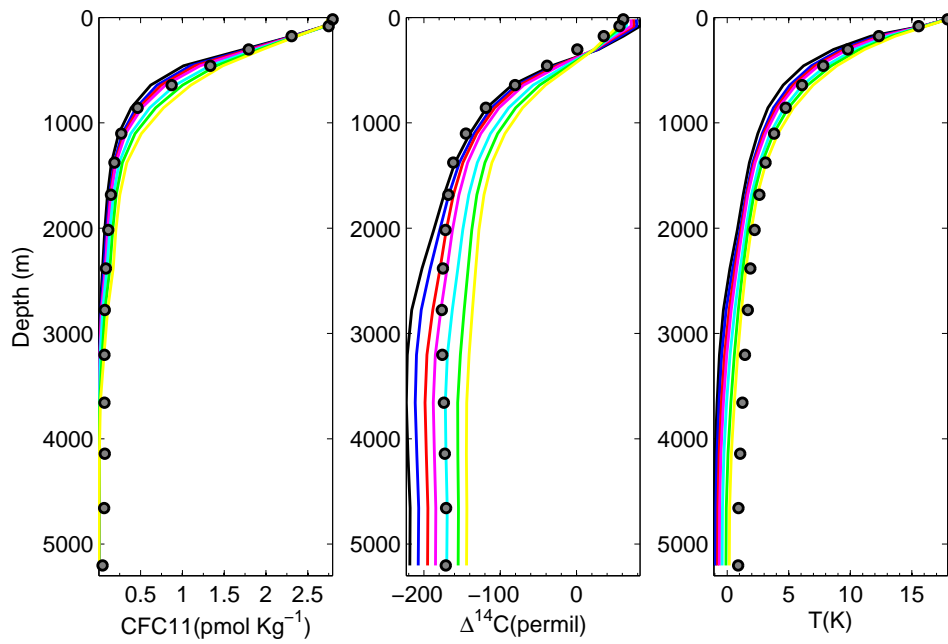


Figure 4. Global averaged profiles of CFC-11 [Key *et al.*, 2004], $\Delta^{14}\text{C}$ [Key *et al.*, 2004] and T [Locarnini *et al.*, 2006], for the observations (gray dots) and model ENSEMBLE 1 (colored lines). The legend for the model K_{bg} values is the same as in Figure 1.

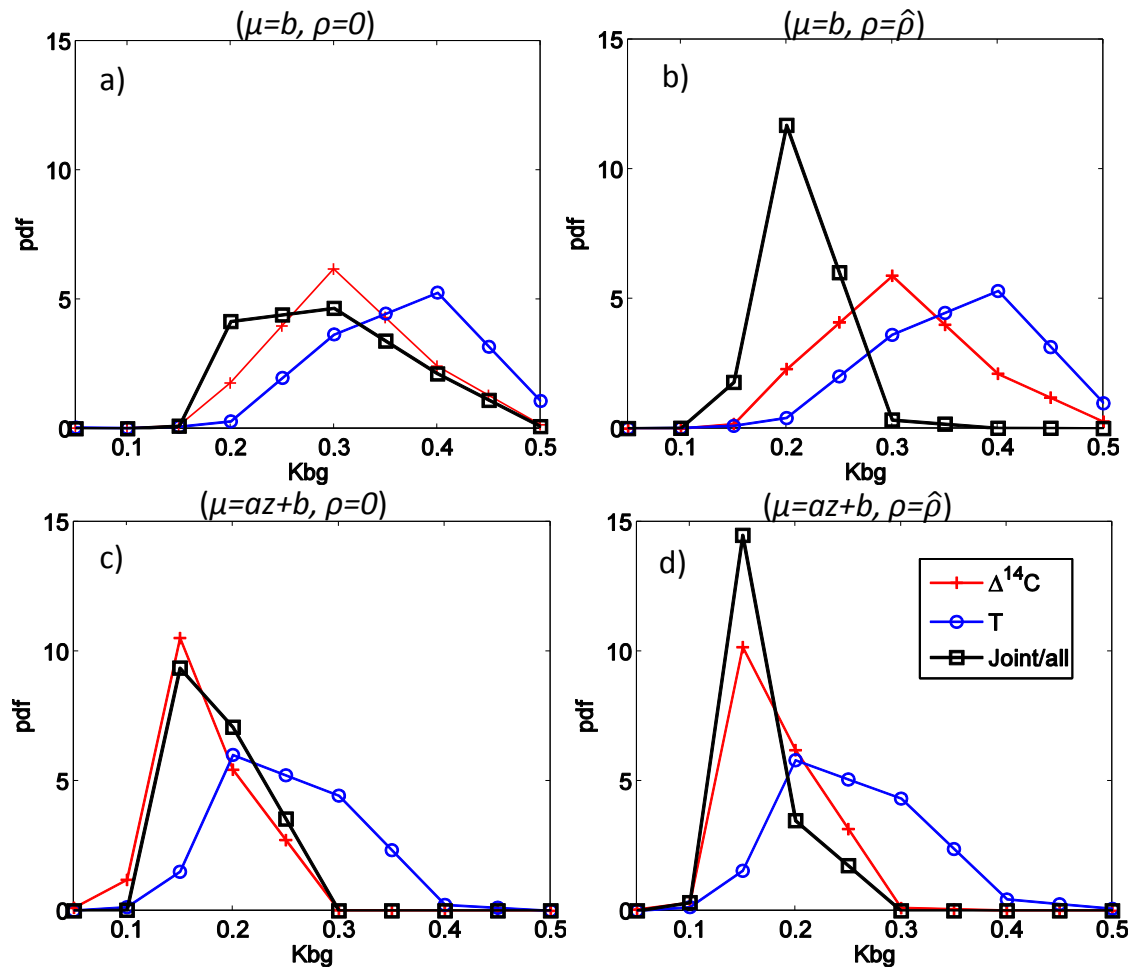


Figure 5. Sensitivity of the model parameter estimation to different treatments of structural model errors. Shown are the posterior probability density function of $\Delta^{14}\text{C}$ (red lines with crosses) and T (blue lines with circles), and the joint posterior using both observations (black line with squares). The panels are for the cases discussed in the text: a) $\mu = b$; b) $\mu = b$ and ρ c) $\mu = az + b$; d) $\mu = az + b$ and ρ .

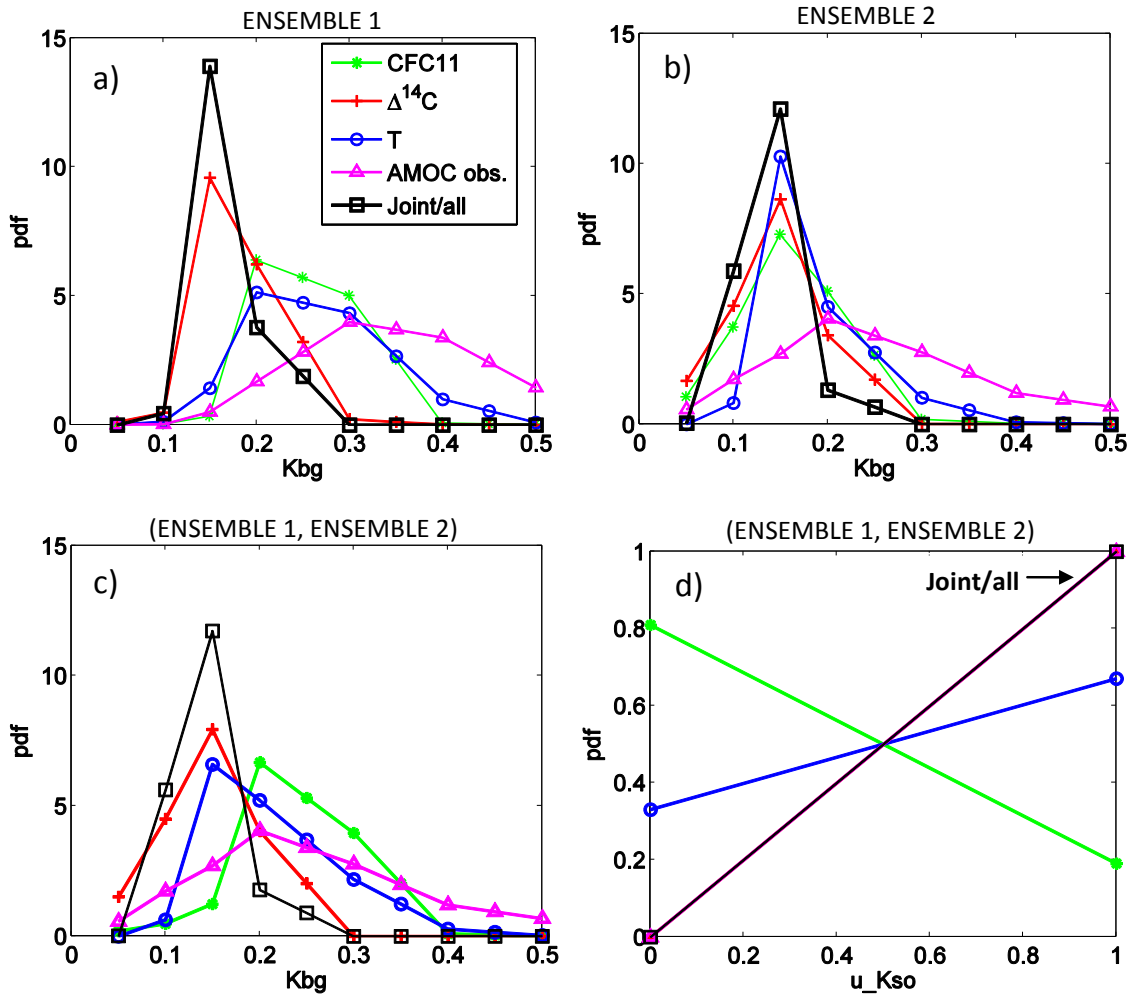


Figure 6. Posterior probability density function of the model parameters for all considered sources of information, the joint posterior using all available information from observations (line with squares). The climatological AMOC estimate of [Lumpkin & Speer, 2003] is plotted for comparison (line with triangles). The K_{bg} estimates are for a) ENSEMBLE 1, b) ENSEMBLE 2, c) ENSEMBLE 1 + ENSEMBLE 2; d) the $u_{K_{SO}}$ estimate is for ENSEMBLE 1 + ENSEMBLE 2

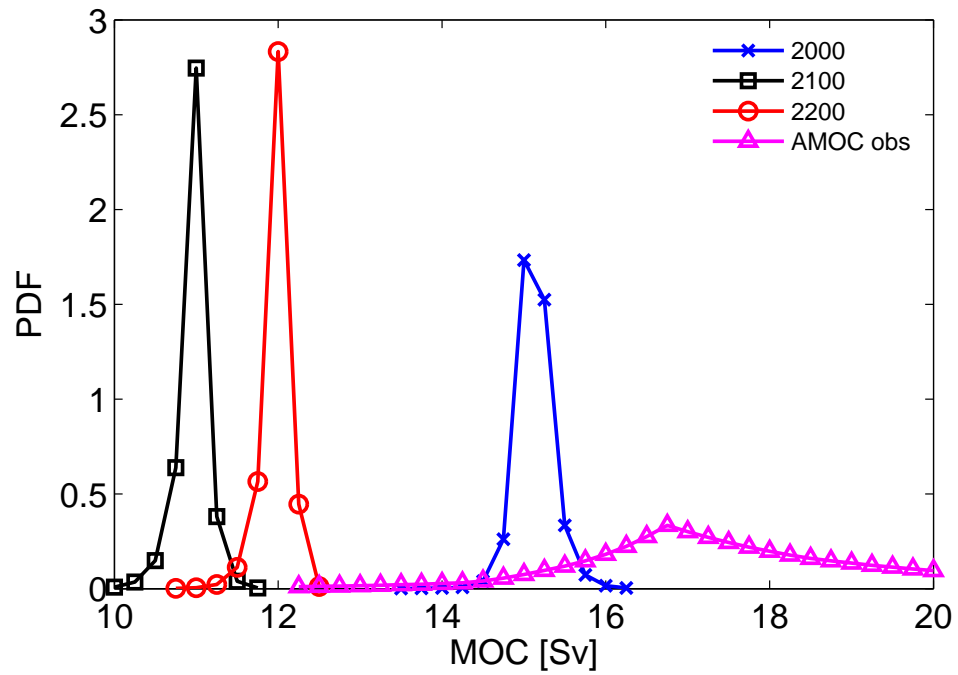


Figure 7. Joint posterior probability density function of model projections of the maximum AMOC strength in the years 2000, 2100 and 2200 using information from the $\Delta^{14}\text{C}$, CFC-11 and T observations. The climatological AMOC estimate of [Lumpkin & Speer, 2003] is added for comparison (line with triangles).